SUPPLEMENTARY INFORMATION

Multiplexed protein force spectroscopy reveals equilibrium protein folding dynamics and the low-force response of von Willebrand factor

Achim Löf [a], Philipp U. Walker [a], Steffen M. Sedlak [a], Sophia Gruber [a], Tobias Obser [b], Maria A. Brehm [b], Martin Benoit [a,1], and Jan Lipfert [a,1]

[a]Department of Physics and Center for NanoScience, LMU Munich, 80799 Munich, Germany
[b]Department of Pediatric Hematology and Oncology, University Medical Center Hamburg-Eppendorf, 20246 Hamburg, Germany

The Supplementary Information contains SI Materials and Methods and Figures S1-S17

Figure S1	Magnetic tweezers setup
Figure S2	Force calibration of the MT setup
Figure S3	Efficient surface passivation by ELP linkers
Figure S4	Constant force measurements at 65 pN
Figure S5	Force-dependence of extension and extension fluctuations of ELP tethers
Figure S6	ELP-based protein attachment strategies
Figure S7	Extension of ELP linker-protein tethers
Figure S8	Determination of rates from the observed unfolding and refolding events
Figure S9	144 h-long measurement of ddFLN4 unfolding and refolding
Figure S10	ddFLN4 does not exhibit hysteresis upon repeated unfolding and refolding
Figure S11	Dissociation of D4-mediated intermonomer interaction in VWF dimers
Figure S12	Measurements on VWF dimers with deletion of the D4 domain
Figure S13	ddFLN4 unfolding and refolding under varied salt and pH conditions
Figure S14	Refolding of the VWF A2 domain under mechanical load in the absence of Ca^{2+}
Figure S15	Occasional inhibition of A2 refolding in VWF dimer tethers
Figure S16	VWF stem unzipping and zipping at low force
Figure S17	Quantification of fast transitions in the VWF stem at low forces

SI Materials and Methods

Preparation of ddFLN4 constructs

Recombinant ddFLN4 expressed in *E.coli* (with the internal cysteine at position 18 mutated to serine) was a kind gift from Lukas Milles (LMU Munich). At its C-terminus, the ddFLN4 construct possesses a polyhistidine-tag for purification and a ybbR-tag(1). At its N-terminus, the construct has a short linker sequence (*MGTGSGSGSGSAGTGSG*) with the terminal methionine followed by a single glycine. Due to efficient cleavage of the methionine by *E.coli* methionine aminopeptidases, the glycine is expected to be available for sortase-catalyzed ligation. The ddFLN4 gene was synthesized codon-optimized for expression in *E.coli* as a linear DNA fragment (GeneArt – ThermoFisher Scientific, Regensburg, Germany), and inserted into pET28a Vectors via Gibson assembly (2) (New England Biolabs, Frankfurt, Germany). Protein expression in *E.coli NiCo21 (DE3)* (New England Biolabs) and purification via the polyhistidine-tag were carried out as previously described in detail (3). For control measurements with an inverted attachment geometry (*cf.* **Supplementary Fig. S6**), an analogous ddFLN4 construct with an N-terminal ybbR-tag and a C-terminal LPETGG sequence was employed.

Preparation of hetero-bifunctional VWF dimer constructs

For preparation of hetero-bifunctional VWF dimers two different types of monomers were co-expressed, which at their N-termini –subsequent to a required signal peptide– possess either a ybbR-tag (1) or an N-terminal strep-tag II for purification (4), followed by a tobacco etch virus (TEV) protease cleavage site (5) and the sortase motif *GG*(6). The TEV site serves two purposes: first, to remove the strep-tag after purification, as it might otherwise interact with Streptavidin on the magnetic beads during measurements, and second, to free the sortase motif *GG*, which must be located terminally for the sortase reaction. Both monomer constructs lack the VWF pro-peptide (domains D1 and D2) in order to abolish linkage of dimers into larger multimers. For delD4 dimers, additionally the D4 domain is deleted in both monomers. For AFM images shown in Fig. 5, dimeric VWF constructs consisting of two identical monomers, possessing a Strep-tag at their N-termini, were used.

Plasmid construction was carried out analogously to a procedure previously described(7). For expression, $2 \cdot 10^6$ HEK 293 cells in a 75 cm^2 flask (DSMZ, Braunschweig, Germany) were transfected in Dulbecco's modified Eagle's medium (Life Technologies, Darmstadt, Germany) containing 10% fetal bovine serum (Life Technologies), 2 µg of each of the two plasmids, and 15 µl Lipofectamine 2000 (Life Technologies). 24 h after transfection,

cells were transferred into selection medium containing 500 µg/ml G418 (Invivogen, Toulouse, France) and 250 µg/ml Hygromycin B (Invivogen). After 2–3 weeks, the polyclonal cell culture was seeded for expression. After 72 h of cell growth, the medium was exchanged against OPTIPRO-SFM (Life Technologies) for serum-free collection of secreted recombinant VWF. The culture supernatant was collected after 72 h and concentrated using Amicon Ultra-15 MWCO 100 kDa (Merck, Schwalbach, Germany).

Dimeric constructs were purified via a HiTrap StrepTrap affinity chromatography column (GE Healthcare) using the AEKTA Explorer system (GE Healthcare). As running buffer, 20 mM 4-(2-hydroxyethyl)-1-piperazineethanesulfonic acid (HEPES), 150 mM NaCl, 1 mM $MgCl_2$, 1 mM $CaCl_2$, pH 7.4, was used. Elution buffer additionally contained 2.5 mM d-desthiobiotin. Eluates were buffer exchanged (to the running buffer) and concentrated by centrifuge filtration using Amicon Ultra MWCO 100 kDa (Merck Millipore). All purified VWF dimers were further inspected by AFM imaging and showed no structural differences as compared to dimeric VWF constructs with different peptide tags or without tags used in previous studies (7, 8).

Preparation of ELP linkers

Recombinant ELP linkers expressed in *E.coli NiCo21 (DE3)* were a kind gift from Wolfgang Ott (LMU Munich). The ≈300 aa ELP linker with a contour length of ≈120 nm used in this study has the sequence $[(VPGEG)\text{-}(VPGVG)_4\text{-}(VPGAG)_2\text{-}(VPGGG)_2\text{-}(VPGEG)]_6$ and possesses a single N-terminal cysteine and the C-terminal sortase recognition motif *LPETGG*. Cloning, expression and purification have been described (9, 10), and can be performed using standard procedures for the production of recombinant proteins. Plasmids are provided at Addgene by Ott et al. (Addgene accession number 90472 for the ELP linker used in this study). For control measurements with an inverted attachment geometry (*cf.* **Supplementary Fig. S6**), analogous ELP linkers with an N-terminal glycine repeat sequence GGG and a single C-terminal cysteine were employed.

Attachment chemistry and flow cell preparation

Functionalization of glass slides with the ELP linkers described above followed the protocol by Ott et al. (9). Glass slides were first silanized with 3-(aminopropyl)dimethylethoxysilane (APDMES, ABCR GmbH, Karlsruhe, Germany), and then coated with 10 mM of a sulfosuccinimidyl 4-(N-maleimidomethyl)cyclohexane-1-carboxylate cross-linker with a negligible contour length of 0.83 nm (Sulfo-SMCC, Thermo Fisher Scientific Inc.), dissolved

in 50 mM HEPES, pH 7.5. Subsequently, ELP linkers were linked to the thiol-reactive maleimide groups via the single cysteine at their N-terminus in coupling buffer consisting of 50 mM sodium phosphate, 50 mM NaCl, 10 mM EDTA, pH 7.2. Afterwards, 10 mM L-cysteine dissolved in coupling buffer were added to saturate potentially remaining unreacted maleimide groups. Finally, non-magnetic polystyrene beads (Polybead Microspheres 3 µm; Polysciences GmbH, Hirschberg, Germany) suspended in ethanol were baked onto the slides at ≈70 °C for ≈5 min for use as reference beads. After each step, slides were extensively rinsed with ultrapure water. Flow cells were assembled from an ELP-functionalized cover slip as the bottom surface and a non-functionalized cover slip with two small holes for inlet and outlet as the top, with a layer of cut-out parafilm (Pechiney Plastic Packaging Inc., Chicago, IL) as a spacer to form a (~4 mm wide and 50 mm long) flow channel. Flow cells were assembled by heating on a hot plate to ≈70 °C for ≈2 min. Assembled flow cells can be stored under ambient conditions for weeks.

Prior to experiments, the flow cells were incubated with 1% casein solution (Sigma-Aldrich) for 1 h and afterwards flushed with 1 ml (approximately 20 flow cell volumes) of buffer (20 mM HEPES, 150 mM NaCl, 1 mM $MgCl_2$, 1 mM $CaCl_2$, pH 7.4). CoA-biotin (New England Biolabs) was coupled to the ybbR-tag on the protein of interest in a bulk reaction in the presence of 5 µM sfp phosphopantetheinyl transferase and 10 mM $MgCl_2$ at 37 °C for 60 min. In the case of VWF, subsequently TEV protease was added to a final concentration of approximately 25 µM and incubated for 30-60 min. Dithiothreitol (DTT) present in the storage buffer of TEV protease was removed beforehand using desalting columns (Zeba Spin 40 K MWCO, Thermo Scientific Inc.). Afterwards, protein was diluted to a final concentration of approximately 10 nM (VWF dimers) or 25 nM (ddFLN4) in 20 mM HEPES, 150 mM NaCl, 1 mM $MgCl_2$, 1 mM $CaCl_2$, pH 7.4, and incubated in the flow cell in the presence of 1-2 µM sortase A for 30 min. Subsequently, the flow cell was flushed with 1 ml of buffer.

Magnetic beads –either Dynabeads M-270 streptavidin (Invitrogen) or beads functionalized with monovalent streptavidin (see below)– in measurement buffer containing 0.1% (v/v) Tween-20 (Sigma-Aldrich) were incubated in the flow cell for 60 s, and unbound beads were flushed out with 2 ml of measurement buffer. All measurements were performed at room temperature (≈22 °C).

Starting with silanized glass slides, complete flow cell preparation takes less than 7 h. In addition, flow cells functionalized with ELP linkers, but not yet incubated with casein and protein, can be prepared in advance and stored at room temperature for weeks without loss of

functionality. Starting with ELP-functionalized flow cells, measurements can be started within 120 min.

Preparation of monovalent streptavidin

Tetrameric, but monovalent streptavidin (mSA) consisting of three mutant subunits deficient in biotin binding and one functional subunit, possessing at its C-terminus a polyhistidine-tag for purification and a single cysteine for site-specific immobilization, was prepared as described in detail by Sedlak et al. (11, 12). In brief, functional and mutant subunits were cloned into pET vectors (Novagen, EMD Millipore, Billerica, USA) and separately expressed in *E.coli BL21(DE3)-CodonPlus* (Agilent Technologies, Santa Clara, USA). Resulting inclusion bodies were solubilized in 6 M guanidine hydrochloride. Functional and mutant subunits were then mixed at a 1:10 ratio prior to refolding and purification via the polyhistidine-tag, in order to ensure a 1:3 ratio of functional to non-functional subunits in the final tetrameric streptavidin construct.

Site-specific, covalent immobilization of monovalent streptavidin on magnetic beads

Magnetic beads with surface amine groups (Dynabeads M-270 Amine, Invitrogen; these beads are otherwise identical to Dynabeads M-270 Streptavidin) were functionalized with 25 mM of 5-kDa NHS–polyethylene glycol (PEG)–maleimide linkers with reactive NHS and maleimide end groups (Rapp Polymere, Tübingen, Germany) in 50 mM HEPES, pH 7.5, and afterwards extensively washed first with DMSO and then with water. The mSA constructs possessing a single cysteine as described above were reduced with 5 mM TCEP bond breaker solution (Thermo Fisher) and afterwards buffer exchanged to coupling buffer using desalting columns (Zeba Spin 40 K MWCO, Thermo Scientific Inc.). Beads were then incubated with mSA in coupling buffer for 90 min and extensively washed with measurement buffer.

Magnetic tweezers setup

Measurements were performed on a custom MT setup described by Walker et al. (13). A schematic and an image of the setup are given in **Supplementary Fig. S1.** The setup uses a pair of permanent magnets (5×5×5 mm^3 each; W-05-N50-G, Supermagnete, Switzerland) in vertical configuration (14). The distance between magnets and flow cell (and, therefore, the force; **Supplementary Fig. S2**) is controlled by a DC-motor (M-126.PD2; PI Physikinstrumente, Germany). For illumination, an LED (69647, Lumitronix LED Technik GmbH, Germany) is used. Using a 40x oil immersion objective (UPLFLN 40x, Olympus,

Japan) and a CMOS sensor camera with 4096×3072 pixels (12M Falcon2, Teledyne Dalsa, Canada), a large field of view of approximately 440 × 330 μm^2 can be imaged at a frame rate of 58 Hz. For measurements with an acquisition rate of 1 kHz, a reduced field of view of 1792 × 280 pixels was used. Images are transferred to a frame grabber (PCIe 1433; National Instruments, Austin, TX) and analyzed with an open-source tracking software (15). The bead tracking accuracy of our setup was determined to be ≈0.6 nm in (*x, y*) and ≈1.5 nm in *z* direction, as determined by tracking non-magnetic polystyrene beads, with a diameter comparable to M270 beads (3 μm), after baking them onto the flow cell surface. For creating the look-up table required for tracking the bead positions in *z*, the objective is mounted on a piezo stage (Pifoc P-726.1CD, PI Physikinstrumente). Force calibration was performed as described by te Velthuis et al. (16) based on the fluctuations of long DNA tethers. The final force calibration, i.e. the dependence of the force applied to a bead on the distance between magnets and flow cell, is shown in **Supplementary Fig. S2**, together with an example trace showing the DNA B-S overstretching transition at the expected force of ≈65 pN. Importantly, for the small extension changes on the length scales of our protein tethers, the force stays constant to very good approximation, with the relative change in force due to tether stretching or protein (un-)folding being < 10^{-4} (**Supplementary Fig. S2**). We verified the uniformity of the magnetic field across the field of view and found the change in force across the full range of the field of view to be < 3% (**Supplementary Fig. S2**). The largest source of force uncertainty is the bead-to-bead variation, which we found to be on the order of ≤ 10% for the beads used in this study (**Supplementary Fig. S2**), in line with several previous reports (14, 17, 18).

AFM imaging

For AFM imaging, a dimeric VWF construct possessing a strep-tag at both N-termini was used. Preparation of substrates for AFM imaging was performed as recently described (7, 8). In brief, 5 μg/ml of VWF dimers in near-physiologic buffer were incubated on a poly-L-lysine-coated mica substrate for 30 s, which was subsequently rinsed with water and finally dried in a gentle stream of nitrogen. AFM images of 1 μm x 1 μm and 1024 x 1024 pixels were recorded in tapping mode in air, using an MFP-3D AFM (Asylum Research, Santa Barbara, CA) and cantilevers with silicon tips (AC160TS, Olympus, Japan), possessing a nominal spring constant of 26 N/m and a resonance frequency of approximately 300 kHz. Raw image data were processed using SPIP software (v6.5.1; Image Metrology, Denmark).

Image processing involved plane correction (third order polynomial plane-fitting), line-wise flattening (according to the histogram alignment routine), and Gaussian smoothing.

Data analysis

All data analysis was carried out using custom-written Matlab scripts (Matlab v.R2015b; The MathWorks Inc., Natick, MA) incorporated into a custom Matlab GUI. We obtained tether extension *vs.* time by subtracting the *z*-position of the reference bead from the *z*-position of the protein-tethered bead. All traces shown and analyzed are the raw extension *vs.* time traces recorded at 58 Hz, used without any filtering or smoothing. For ddFLN4 measurements, only beads that in unfolding force plateaus repeatedly showed a double-step with a short-lived intermediate state were taken into account for further analysis. Similarly, for VWF measurements, only beads repeatedly exhibiting two steps of equal height corresponding to unfolding of the A2 domains in unfolding force plateaus were analyzed, unless otherwise noted. Unfolding and refolding behavior for ddFLN4 and VWF under the different reported buffer conditions were observed in at least 3 independently prepared flow cells in all cases.

To determine the position of folding and unfolding steps, we employed the step-finding algorithm by Kerssemakers et al. (19), and the corresponding change in extension was determined as the difference between the average extensions of the adjacent 1000 frames recorded before and after the step, respectively (fewer frames were used if the 1000-frame interval contained another step). Extensions of folding and unfolding (sub)steps were histogrammed for each clamped force (1 nm binning for ddFLN4, and 3 nm and 2 nm binning for VWF A2 unfolding and refolding, respectively), and fitted with Gaussians. Error bars in figures report the FWHM of the fits, divided by the square root of the respective counts. The resulting force–extension profiles were fitted to the WLC model of polymer elasticity (an approximation to this model with less than 1% relative error was used for fitting (20)). In the case of ddFLN4, a fixed persistence length of 0.5 nm was used to enable direct comparison with results from an AFM study by Schwaiger et al. (21). In the case of VWF A2, both persistence length and contour length were free fit parameters.

To determine the unfolding or refolding rates $k(F)$ at a given constant force F, the respective fraction of observed unfolding or refolding events as a function of time was fitted with the exponential expression $1 - a \exp(-kt) + b$ (**Supplementary Fig. S8**), where the free parameters a and b can compensate for events that were missed due to the finite measurement time or due to the finite time of motor movement when setting the force. However, such missed events were rare and parameters a and b were close to 1 and 0, respectively. Error bars

on rates in figures indicate 95% confidence bounds of fits. In the case of VWF, only events corresponding to steps with extensions ≤ 60 nm were taken into account to ensure that only A2 unfolding events –and not dissociation of the D4-mediated intermonomer interaction (see **Supplementary Fig. S11**)– are analyzed.

The force dependence of unfolding and refolding rates was described by a single barrier kinetic model: $k(F) = k_0 \exp(F\Delta x/k_BT)$, with the rate at zero force k_0 and the distance to the transition state Δx as fit parameters, and k_BT = 4.1 pNnm. Fitting of this exponential model was carried out as a linear fit of the form $c \times F + d$ (with $c = \Delta x/k_BT$ and $d = \ln k_0$) to the natural logarithm of the rate data $\ln k(F)$, employing least-squares fitting using the singular value decomposition algorithm. Error margins for k_0 and Δx given in the text correspond to 1 SD of the fit coefficients c and d.

To obtain step sizes and dwell times of the observed transitions in the C-terminal stem of VWF dimers, we employed the step finding algorithm by Kerssemakers et al. (19). Characteristic times were determined by maximum likelihood fits of a single-exponential model, as described in the main text and the respective figure legends.

For bead rupture measurements, lifetimes at different constant forces were determined from the survival fraction *vs*. time data based on > 35 rupture events for each condition. In the case of mSA-beads, data were described by a single-exponential decay, and the corresponding lifetime was determined by a linear fit to the natural logarithm of the data. In the case of the more complex decay behavior observed for commercial streptavidin-coated beads, lifetimes for the fastest- and slowest-decaying populations were estimated by linear fits to the natural logarithm of the first and last 20% of data points, respectively. The dependence of estimated lifetimes on force was again described by the single barrier kinetic model introduced above.

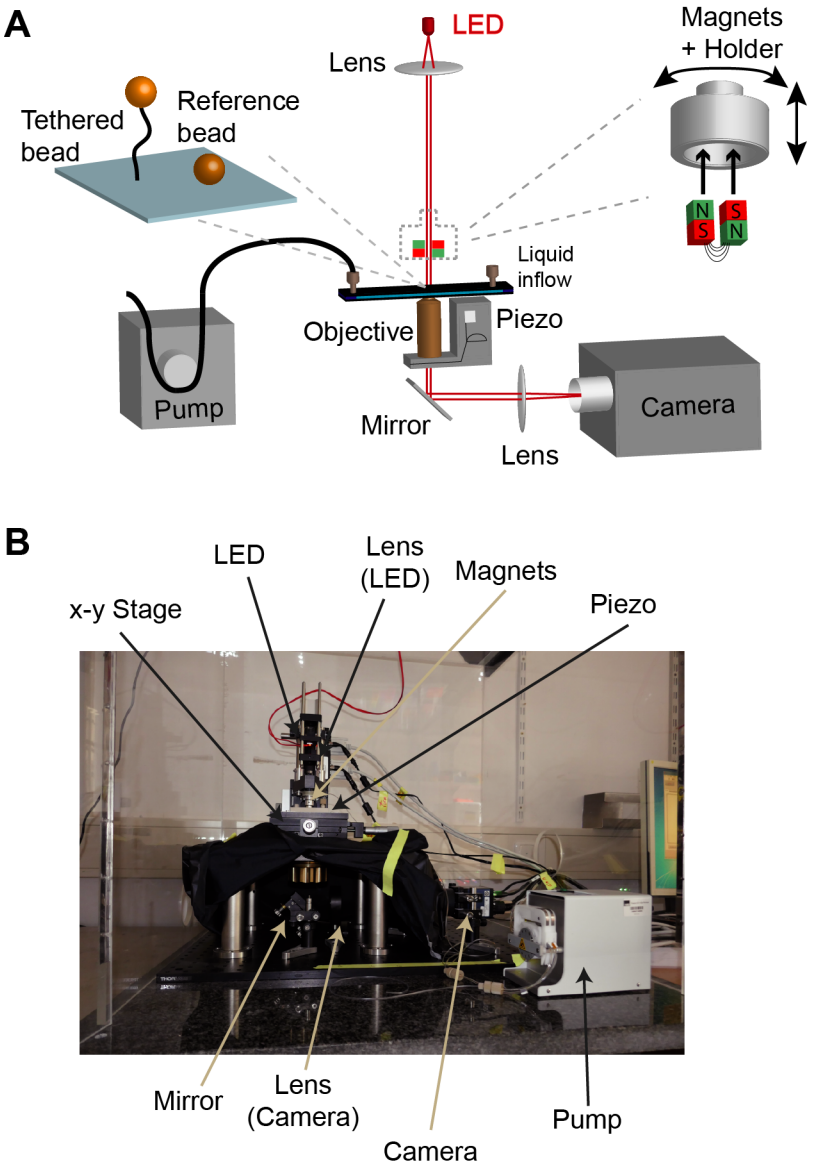

Fig. S1. Magnetic tweezers setup. (A) Schematic of the MT setup. Proteins are tethered between a magnetic bead and the bottom surface of the flow cell, which is illuminated using an LED. A large field of view is imaged using a 40x oil-immersion objective and a CMOS sensor camera. For creating the look-up table necessary to track the *z* position of the beads, the objective is mounted on a piezo stage. A set of two cubic permanent magnets is positioned above the flow cell. The distance between magnets and flow cell can be adjusted using a DC-motor in order to adjust the force applied to the magnetic beads. A peristaltic pump allows for flushing the flow cell. For technical details of the different components, see **Methods**. **(B)** Image of the MT setup with essential components being highlighted.

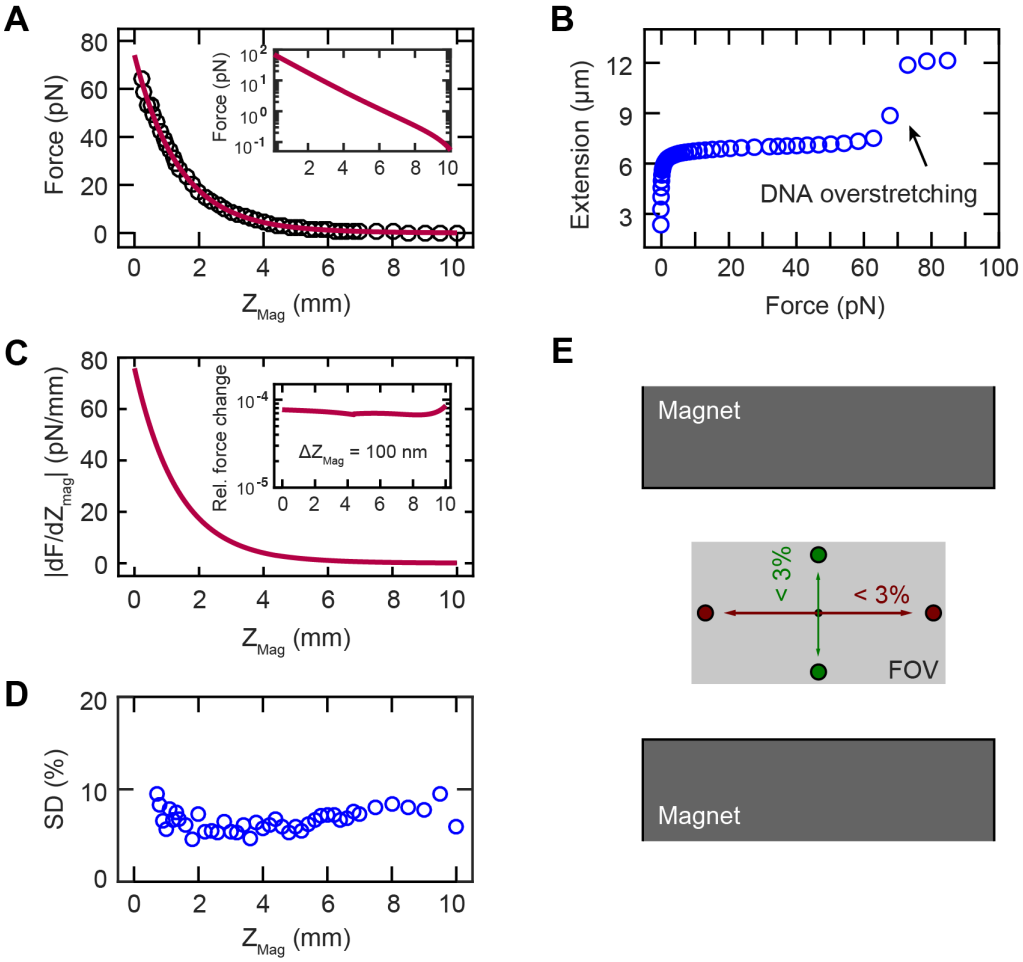

Fig. S2. Force calibration of the MT setup. (A) Force acting on the magnetic beads used in this study (Dynabeads M270) as a function of the distance Z_{Mag} between the magnets and the flow cell. Forces were calibrated using the method described by Velthuis et al. (16), based on the Brownian fluctuations of long (here 21 kbp) double-stranded (ds) DNA tethers. Data points are mean forces determined from 16 DNA tethers. The red line is the final fit of the dependence of force on the magnet distance. **(B)** Exemplary trace of a 21 kbp dsDNA tether, showing the B-S overstretching transition at the expected force of ≈65 pN, confirming the force calibration from analysis of the transverse fluctuations. (**C**) Absolute value of the derivative of the force with respect to Z_{Mag}. The inset shows the relative force change for extension changes in z direction of 100 nm –larger than any (un-)folding steps in our measurements–, which was found to be $< 10^{-4}$ for all forces, as calculated from the expression for $|dF/dZ_{Mag}|$. **(D)** Bead-to-bead force variation. Independently performing the calibration procedure for 16 different DNA tethers, we found the standard deviation of the force from the mean value to be ≲ 10% over the whole range of magnet distances, indicating a bead-to-bead force variation of ≲ 10%, in line with previous reports (14, 17, 18). **(E)** Force uniformity across the field of view. To verify that the magnetic field is uniform and thus the forces do not vary significantly across the field of view (FOV), we repeatedly performed the force calibration procedure for the same DNA tether at different positions at the edges of the FOV, as schematically indicated by circles, and in the middle of the FOV. For each of four independently measured DNA tethers, changes in force were found to be < 3% both along the axis parallel to and the axis perpendicular to the gap between the magnets (not drawn to scale).

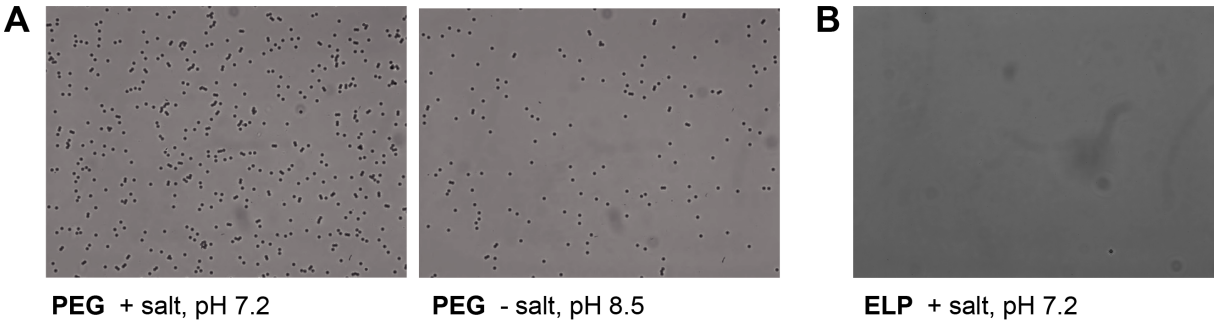

Fig. S3. Efficient surface passivation by ELP linkers. (A) Unspecific binding of streptavidin-coated magnetic beads to a flow cell surface coated with polyethylene glycol (PEG) linkers. As flow cell surface, an amino-silanized glass slide was functionalized with 25 mM of PEG linkers (MW 5 kDa; contour length of approximately 120 nm) via functional NHS groups on one end of the PEG linkers, as routinely performed for, e.g., AFM-based single-molecule force spectroscopy (9, 22, 23). To test the quality of passivation provided by the PEG layer, streptavidin-coated magnetic beads were flushed into the flow-cell in the absence of the protein of interest, incubated for 1 h, and finally the flow cell was flushed extensively with buffer. For buffer close to the desired measurement conditions (approximately neutral pH and containing both monovalent (72 mM NaCl) and divalent (1 mM $CaCl_2$) salts), a very large number of beads remained unspecifically bound to the surface after flushing (left image). Sticking could be reduced, but not eliminated, by adjusting buffer conditions (e.g. at basic pH and in the absence of salt; right image) or by adding detergents and/or further passivation agents such as BSA or casein. **(B)** Efficient passivation by ELP linkers. For flow cell surfaces coated with ELP linkers (see **Methods** section for details of the coupling protocol), essentially no beads (0-1 per FOV) bound unspecifically to the flow cell surface in the absence of the protein of interest.

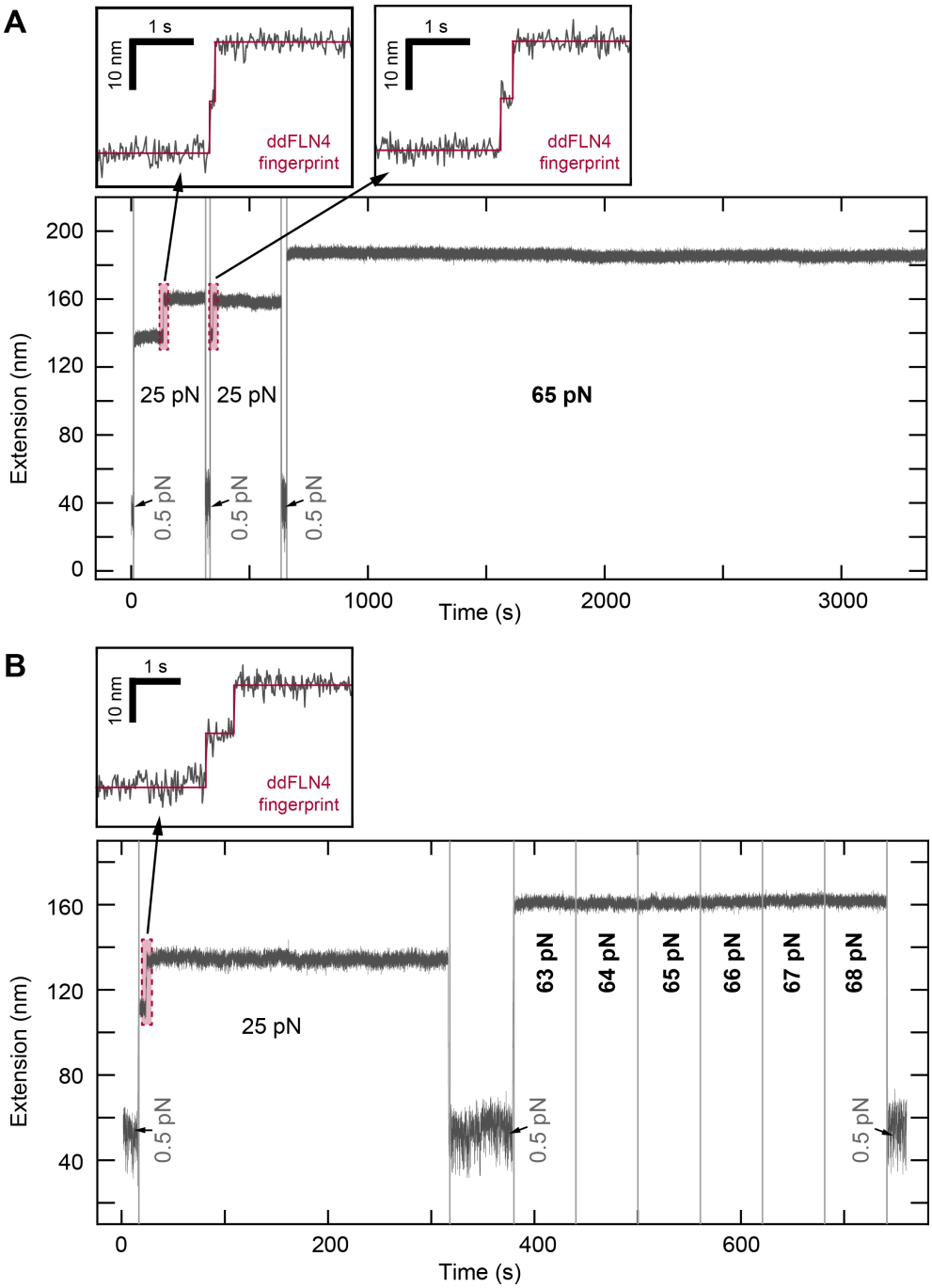

Fig. S4. Constant force measurements at 65 pN. (A,B) Example extension traces of ddFLN4-ELP linker complexes tethered between a glass surface and magnetic bead as shown in Fig. 1 in the main text. Short initial force plateaus of 25 pN reveal the characteristic three-state unfolding of ddFLN4 as a fingerprint to identify specific, single-molecule tethers. Subsequently, tethers were subjected to a constant force of 65 pN for an extended period of time (A) or to stepwise increasing forces in the range from 63 to 68 pN (B). The ELP linkers exhibit a stable extension without any specific features in this force range. In contrast, DNA linkers exhibit the DNA overstretching overstretching transition in this force range (**Fig. S2B**), which would interfere with measurements.

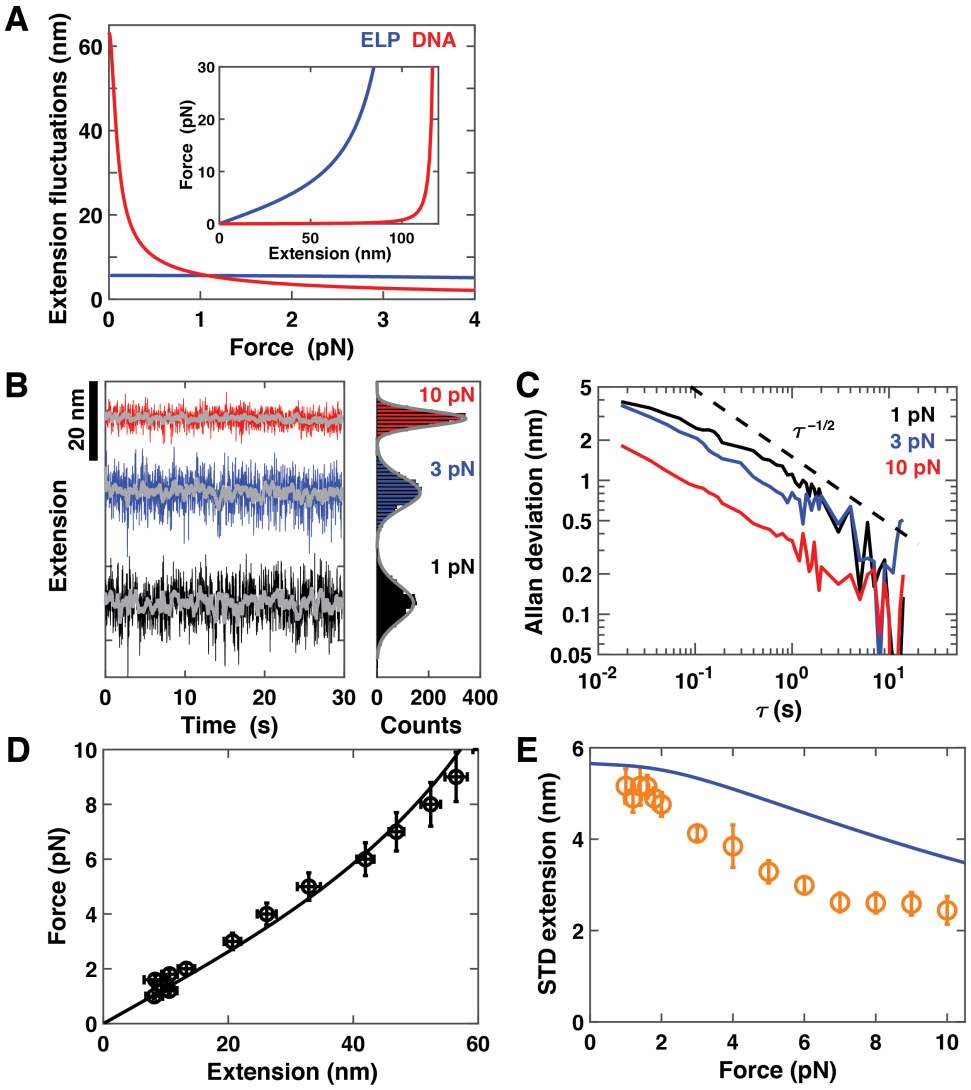

Fig. S5. Force-dependence of extension and extension fluctuations of ELP tethers. (A) Predictions of the extension fluctuations of an ELP linker (blue) and double-stranded DNA (red) assuming a contour length of 120 nm for both molecules and a bending persistence length of 0.4 and 50 nm for the ELP and DNA, respectively. In the MT, the extension fluctuations are given by $\sigma_Z = (k_BT / (\partial F/\partial L))^{1/2}$ where k_BT is the thermal energy (24) and we approximate $\partial F/\partial L$ from the derivative of the worm-like chain model using the parametrization of Ref. (25). Inset: Predicted force-extension relationships for an ELP linker and a double-stranded DNA using the same parameters and WLC parameterization as in the main panel. The lower slope in the force vs. extension plot for DNA compared to the ELP at low forces is apparent and gives rise to the higher level of extension fluctuations σ_Z for DNA at low forces. **(B)** Example extension vs. time traces and extension histograms of an ELP linker (coupled to folded ddFLN4) at 1, 3 and 10 pN. Colored data are raw data recorded at 58 Hz. Grey lines are data smoothed to 3 Hz. The extension histograms are well described by Gaussian distributions (dark grey lines). Traces and histograms are vertically offset for clarity. **(C)** Allan deviations (ADs) of the traces shown in panel B. The AD is defined as the square root of one-half of the averaged square distance between the means of neighboring intervals of length τ (26–28). Intuitively, the AD gives a measure of the spatial resolution after averaging over a time interval τ. We note that for the current data set, we do not resolve the initial maximum in the AD, since the characteristic frequency of the fluctuations (i.e. the corner frequency) is faster than the camera frequency of 58 Hz. The AD decreases with increasing force, due to the higher stiffness of the system at higher forces, and decreases with increasing averaging time τ. For our data, the decrease of AD with τ follows the $\tau^{-1/2}$ behavior

(indicated by the dashed line) expected for the averaging of thermal fluctuations up to $\tau \sim 5$ s; for larger τ, drift becomes noticeable in the data and the AD deviates from the $\tau^{-1/2}$ trend. **(D)** Mean tether extension as a function of applied stretching force for an ELP tether. Error bars on the extension were obtained by dividing the extension traces in 4 equal segments and computing the standard deviation over the respective means. The error bars on the forces are 10% of the force. The black line is a prediction of the WLC with contour length 120 nm and bending persistence length 0.4 nm. **(E)** Standard deviation of the extension fluctuations of an ELP tether as a function of applied force. Error bars were obtained by dividing the extension traces in 4 equal segments and computing the standard deviation over the respective standard deviations. Force error bars were omitted for clarity. We note that the level of the extension fluctuations is close to the predictions in panel A (shown as a blue line), both in terms of the absolute level and in terms of the weak force dependence. However, the experimental data can not be directly compared to the predictions, since the camera effectively filters the extension data (see panel C), causing the data points to lie below the theoretical prediction from panel A.

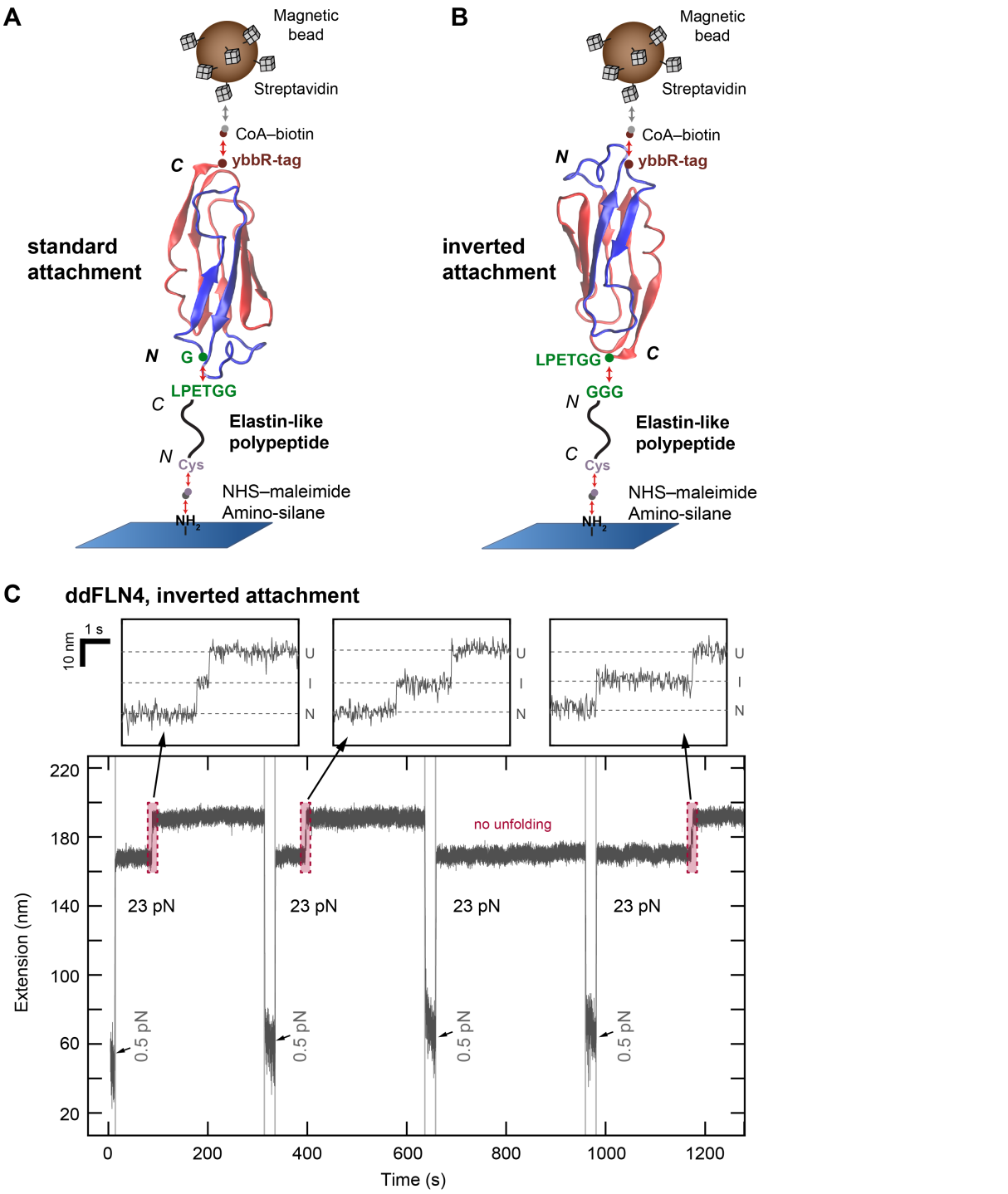

Fig. S6. ELP-based protein attachment strategies. (A) Attachment geometry as presented in Fig. 1 in the main text and employed for all measurements presented in the main text and Supplementary Information (not to scale). The protein of interest (here ddFLN4 is shown), with an N-terminal glycine and a C-terminal ybbR-tag, is coupled to an ELP linker carrying a C-terminal LPETGG motif and an N-terminal cysteine. **(B)** Inverted attachment geometry. The protein of interest, now with an N-terminal ybbR-tag and a C-terminal LPETGG motif, is coupled to an ELP linker carrying an N-terminal glycine repeat sequence GGG and a C-terminal cysteine. **(C)** Exemplary extension trace of a ddFLN4-ELP tether attached in the inverted geometry presented in panel B, repeatedly showing the characteristic three-state unfolding signal of ddFLN4. We found comparable yields of specific, single-molecule tethers for the two different attachment geometries.

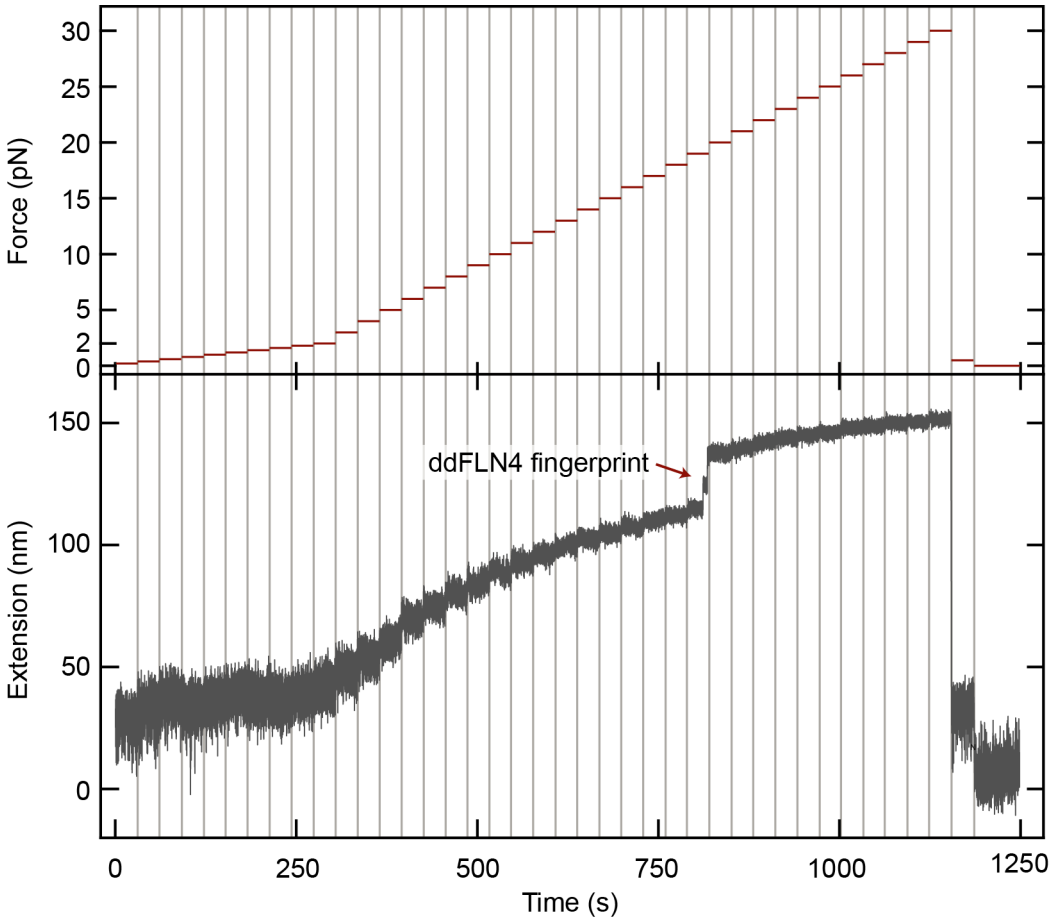

Fig. S7. Extension of ELP linker-protein tethers. Exemplary extension trace (bottom) of a ddFLN4-ELP linker complex tethered between glass surface and magnetic bead as shown in Fig. 1 in the main text, recorded while the force was increased stepwise every 30 s (indicated by red lines; top), in steps of 0.2 pN between 0.2 and 2 pN, and in steps of 1 pN between 2 and 30 pN. Afterwards, the tether was relaxed to 0.5 pN to allow for refolding of ddFLN4 and further relaxed to zero force to determine the zero position of extension. No features –in particular no steps– were observed over the entire probed force range, with exception of the characteristic ddFLN4 unfolding pattern, which served to identify specific single-tethered beads. This finding shows that the ELP linker does not cause any signals that may interfere with analysis of the specific signals of the measured protein of interest.

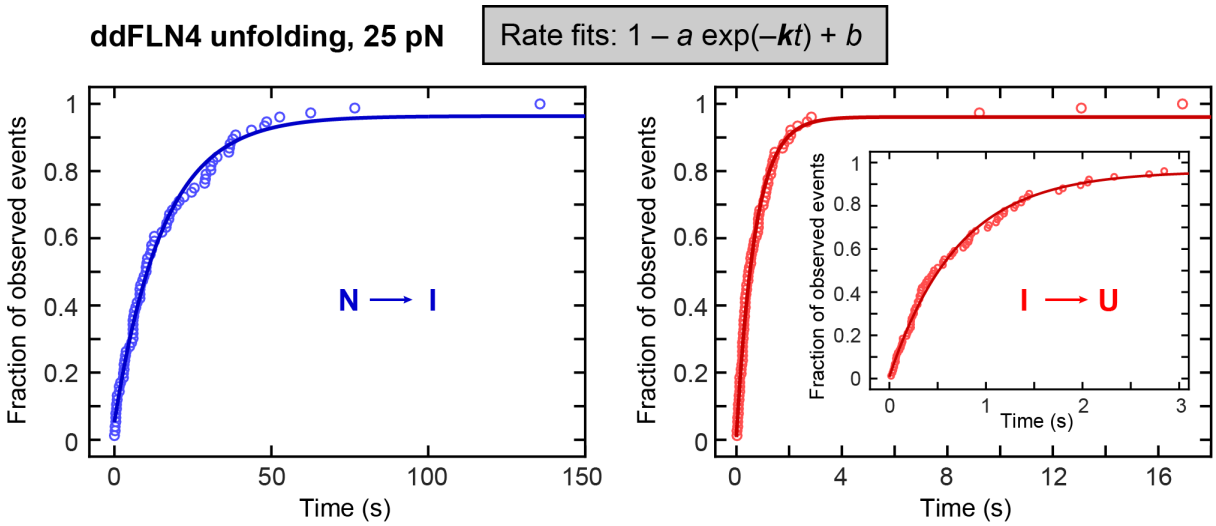

Fig. S8. Determination of rates from the observed unfolding and refolding events. Concept of rate determination from the fraction of observed unfolding or refolding events as a function of time. Shown here as an example are the fractions of observed unfolding events *vs*. time for the two substeps of ddFLN4 unfolding at 25 pN, i.e. for the transitions from the native (N) to the intermediate (I) state (left, blue) and from the intermediate to the unfolded (U) state (right, red). To obtain the unfolding rate k of a transition at constant force F, the fraction of observed unfolding events as a function of time t is fit to the expression $1 - a \exp(-kt) + b$ (lines), where the free parameters a and b can compensate for events that were missed due to the finite measurement time or due to the finite time of motor movement when setting the force. As a rule, parameters a and b were close to 1 and 0, respectively.

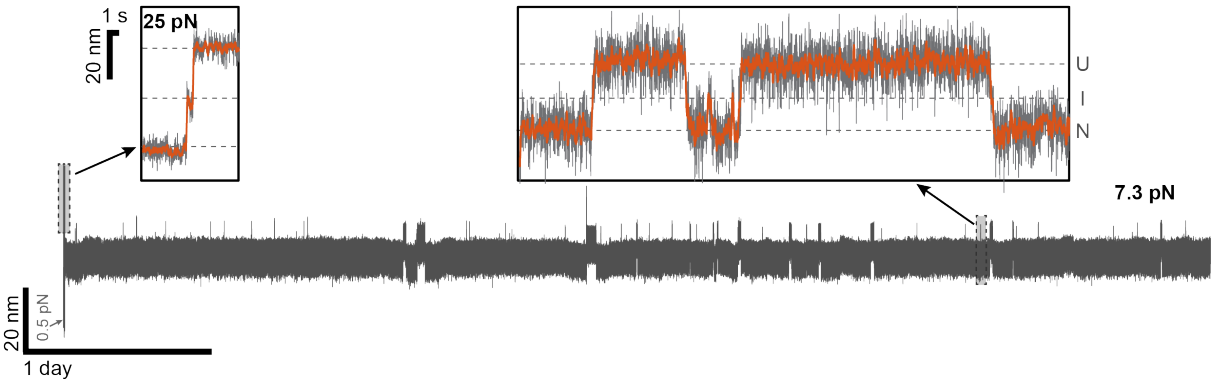

Fig. S9. 144 h-long measurement of ddFLN4 unfolding and refolding. 144 h-long extension *vs.* time trace of a ddFLN4 tether subjected to a constant force of 7.3 pN and zooms into indicated segments of the trace. As in Figure 3, zooms show not only full unfolding and folding transitions, but also transitions from the native to the intermediate state and back. This behavior is found during the whole measurement. Dashed lines indicate average extension levels corresponding to the native (N), intermediate (I), and unfolded (U) states, respectively. As the force is slightly below the equilibrium force, the protein is primarily in its native state. Drift was corrected for by subtracting a reference bead. Long-term drift was removed by subtracting a moving-average filtered trace with a window of 100000 frames. The spike at 40 h is due to debris swimming through the ROI of the reference bead.

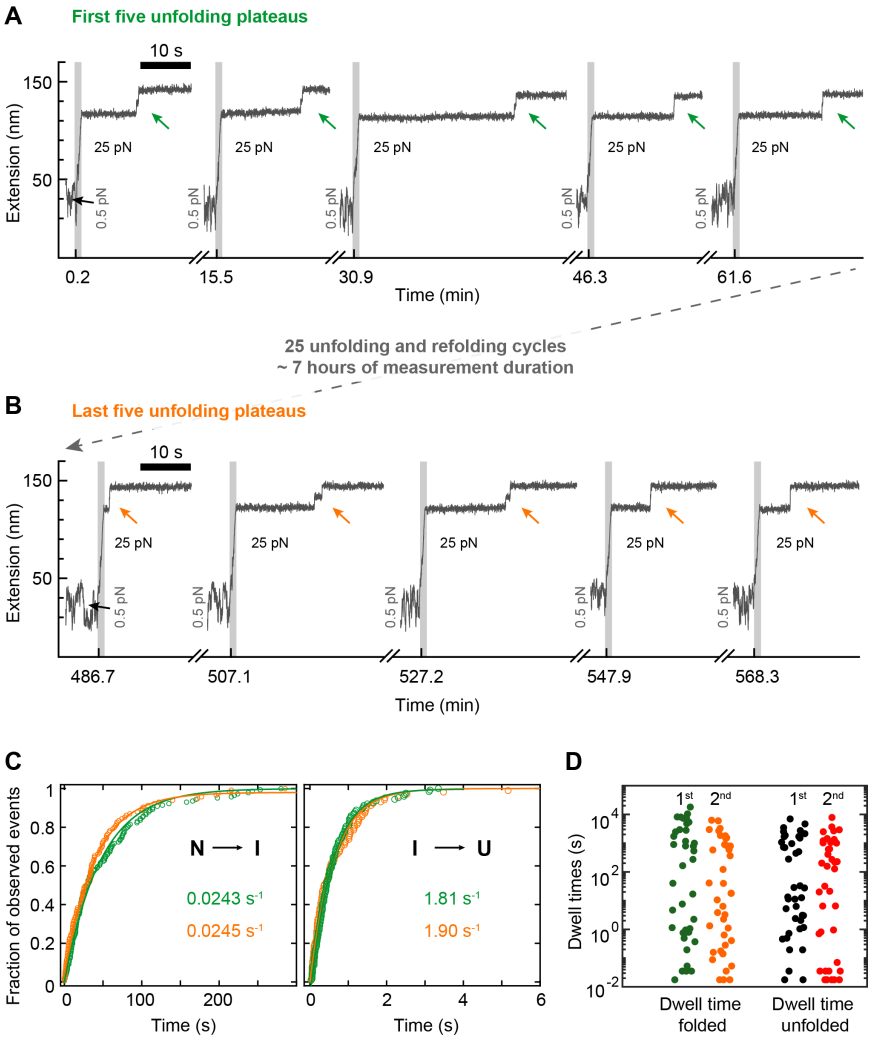

Fig. S10. ddFLN4 does not exhibit hysteresis upon repeated unfolding and refolding. (A,B) Segments from a ≈10 h-long measurement on ddFLN4 tethers with repeated alternating unfolding and refolding plateaus (similar to the data shown in **Fig. 2B**). Reliable unfolding and refolding was observed throughout the entire measurement. Shown here for one exemplary tether are the first five **(A)** and the last five **(B)** unfolding plateaus (all at 25 pN; unfolding events marked by arrows), which were separated by 25 cycles of unfolding and refolding, corresponding to ≈7 h of measurement duration. We analyzed the same 31 ddFLN4 tethers, separately for the first five and last five unfolding plateaus. The obtained mean extension values for the two unfolding transitions N→I and I→U both varied by less than 4%. Furthermore, the measured unfolding rates matched very closely. **(C)** Fits and unfolding rates are shown in green and orange for the first five and last five plateaus, respectively. The rates for the first step of unfolding, N→I (left panel; first five plateaus: 0.0243 [0.0234 - 0.0253] s^{-1}; last five plateaus: 0.0245 [0.0238 - 0.0252] s^{-1} ; mean and 95% confidence intervals), and for the second step of unfolding, I→U (right panel; first five plateaus 1.81 [1.77 - 1.85]; last five plateaus: 1.90 [1.78 - 2.01]), rates deviated by less than 5%, well within the 95% confidence intervals of the fits. Our data thus indicate that no significant hysteresis effects occur for ddFLN4 even after tens of unfolding/refolding cycles and spending an extended period of time in the unfolded state. **(D)** Analysis of a long (~55 h) trace at constant force close to the equilibrium point (the trace shown in **Fig. 3B**). The dwell times in the folded and unfolded states were quantified and are shown separately for the first and second halves of the trace. The distributions for the two halves of the trace for both folded and unfolded states are identical, within experimental error (as assessed by a two-sample Kolmogorov–Smirnov test with $p = 0.51$ and $p = 0.53$, respectively).

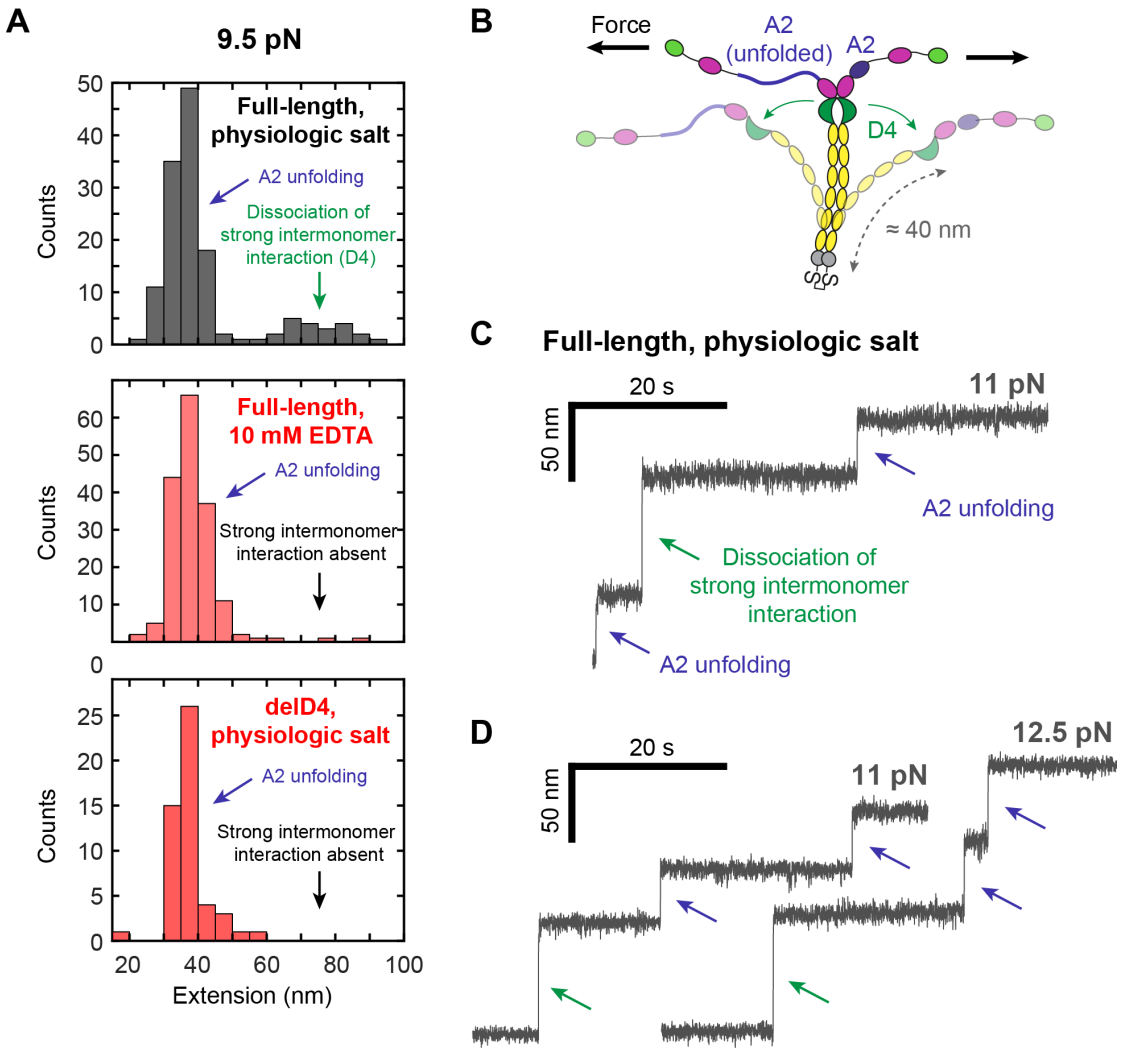

Fig. S11. Dissociation of D4-mediated intermonomer interaction in VWF dimers. (A) Extension histograms of steps observed in traces of VWF dimers recorded at a force of 9.5 pN, for full-length dimers in the presence of divalent ions (top) or in the presence of 10 mM EDTA (middle), and for dimers with a deletion of the D4 domain (delD4, see also **Supplementary Fig. S7**) in the presence of divalent ions (bottom). In the case of the full-length dimers, in the presence of divalent ions a broad peak at extension values of roughly 70-80 nm is observed in addition to the peak associated with A2 unfolding, centered at ca. 36 nm. In the presence of EDTA, or for the delD4 construct, in contrast, only the peak associated with A2 unfolding is observed. The length increase by 70-80 nm, the sensitivity to removal of divalent ions by EDTA, and the involvement of the D4 domain are in line with the dissociation of a strong intermonomer interaction mediated by VWF's D4 domain that has recently been identified in AFM force measurements on VWF dimers (7, 8). **(B)** Schematic of dimer opening. Dissociation of an intermonomer interaction mediated by the D4 domain (green) leads to the opening of the closed stem region of VWF (yellow) and thus a release of formerly hidden length of approximately 80 nm. Dimer opening occurs independently of A2 (blue) unfolding, since the A2 domains are not shielded from force by the D4-mediated interaction. **(C)** Exemplary extension trace of a full-length dimer exhibiting unfolding of both A2 domains and dimer opening, recorded at 11 pN. **(D)** Extension traces from the same VWF dimer tether, probed at different forces and repeatedly exhibiting dimer opening, implying reversibility of the D4-mediated intermonomer interaction.

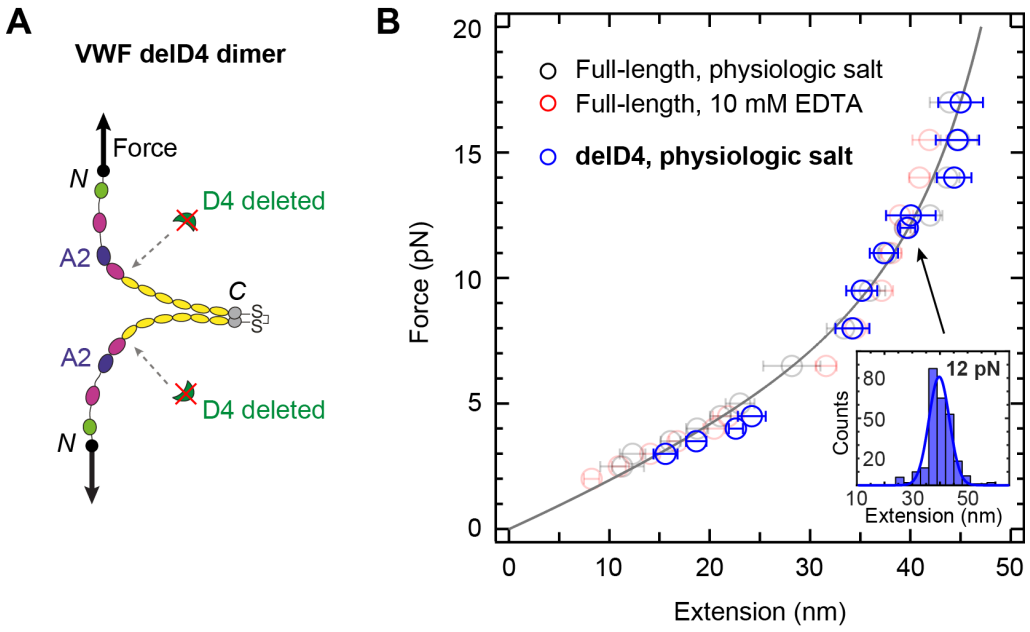

Fig. S12. Measurements on VWF dimers with deletion of the D4 domain. (A) Schematic structure of a VWF dimer with deletion of both D4 domains (delD4 dimer). The two A2 domains are shown in blue. Arrows indicate the direction of force acting on the two N termini during MT experiments. **(B)** Force–extension profile of A2 unfolding and refolding, recorded for the delD4 construct in near-physiologic buffer at pH 7.4 (blue symbols). The force–extension profile closely matches those obtained for the full-length construct in near-physiologic buffer and in buffer with 10 mM EDTA (co-plotted with lower opacity in black and red, respectively), as presented in Fig. 4c in the main text. The line is the global WLC fit to all data from the full-length construct, as presented in the inset in Fig. 4C in the main text. Data points are obtained by Gaussian fits to step extension histograms (inset) at each constant force. Data points above 5 pN are from unfolding, data points up to 5 pN from refolding. Error bars correspond to the FWHM of Gaussian fits, divided by the square root of counts.

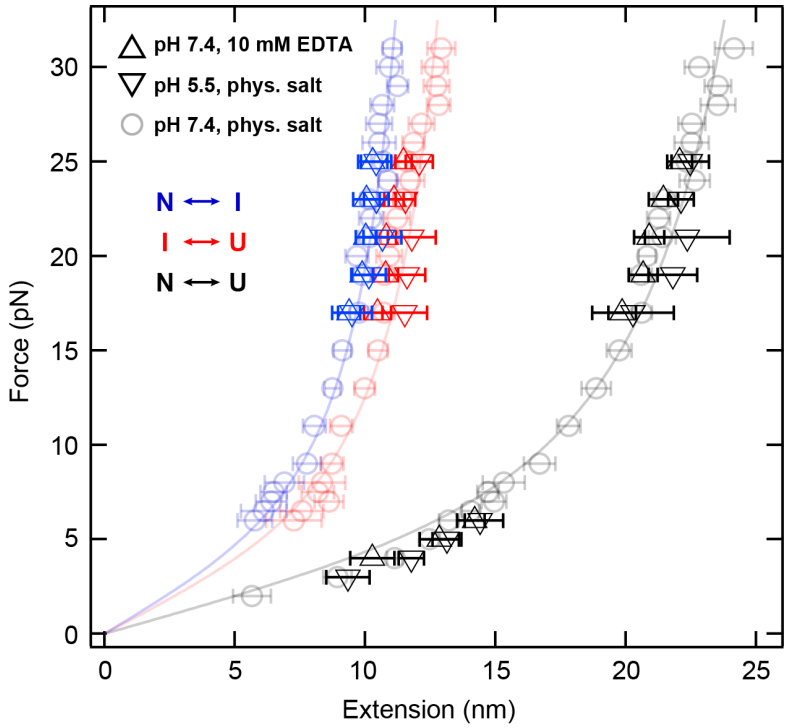

Fig. S13. ddFLN4 unfolding and refolding under varied salt and pH conditions. Extension of ddFLN4 unfolding and refolding steps at different constant forces and under varied buffer conditions. Extensions of the transitions between the native state and the intermediate state (blue) as well as between the intermediate and the unfolded state (red) are shown separately in addition to the full extension between native and unfolded state (black). Data points at forces up to 8 pN are from refolding, data points at forces above 8 pN from unfolding measurements. Co-plotted with lower opacity are the data obtained for near-physiological buffer conditions (pH 7.4, with divalent ions; circles) as shown in Fig. 2c in the main text and the respective WLC fits (lines). Force–extension data sets obtained at pH 7.4 in the presence of 10 mM EDTA (upward triangles) and at acidic pH 5.5 in the presence of divalent ions (downward triangles) both are within measurement uncertainty identical to the ones obtained for near-physiologic buffer conditions. Error bars correspond to the FWHM of Gaussian fits, divided by the square root of counts.

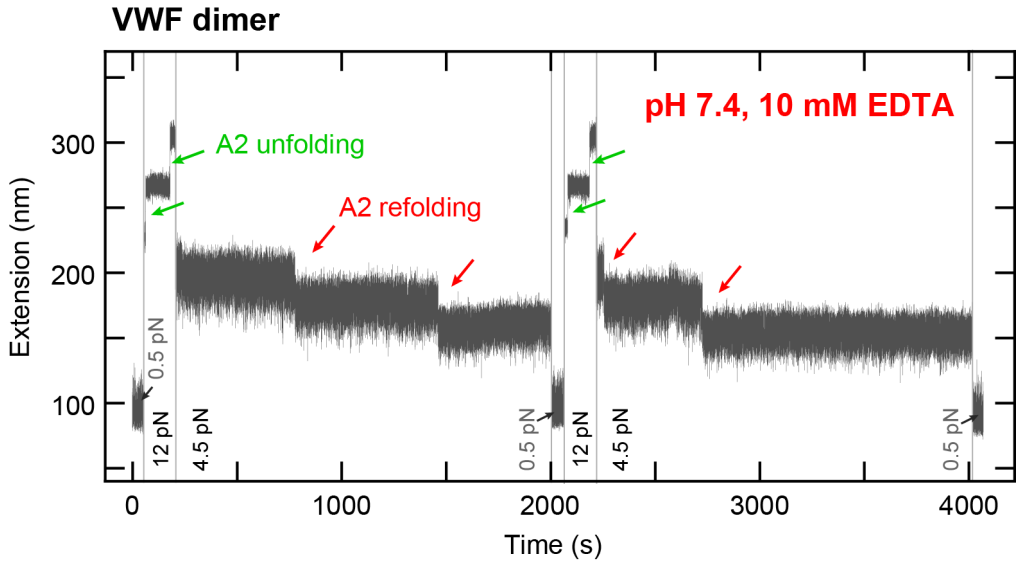

Fig. S14. Refolding of the VWF A2 domain under mechanical load in the absence of Ca^{2+}. Extension *vs.* time trace of a VWF dimer tether subjected to alternating intervals of high force (here 12 pN), allowing for A2 unfolding, of intermediate force (here 4.5 pN), allowing for direct observation of A2 refolding, and of low force (0.5 pN) to ensure refolding, in buffer without Ca^{2+} and with 10 mM EDTA. Unfolding and refolding of the two A2 domains are observed as two independent positive or negative steps in the trace, respectively. Direct observation of refolding steps (marked by red arrows) shows that A2 can refold under significant mechanical load even in the absence of Ca^{2+}.

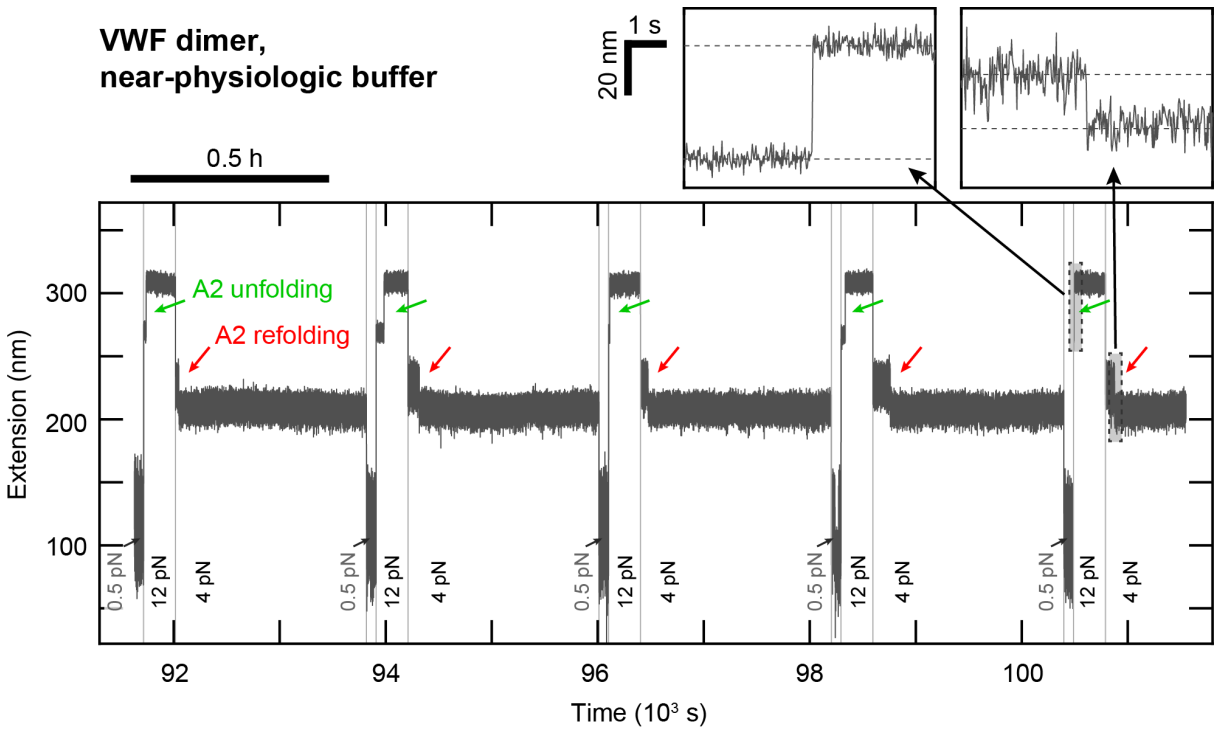

Fig. S15. Occasional inhibition of A2 refolding in VWF dimer tethers. Segment of a ≈30 h-long extension *vs.* time trace of a VWF dimer tether subjected to alternating intervals of high force (here 12 pN), allowing for A2 unfolding, and of different intermediate forces (4 pN shown here), allowing for direct observation of A2 refolding, recorded under near-physiologic buffer conditions. The shown tether exhibits the unfolding and refolding signal (marked by arrows) of only one of the two A2 domains. Otherwise, the tether does not show any differences to regular tethers exhibiting signals of both A2 domains. In particular, the observed A2 unfolding and refolding steps were indistinguishable (see insets). In such tethers exhibiting only one A2 signal, which occurred only occasionally, refolding of one of the A2 domains may be inhibited due to cis-trans isomerization of a cis-proline, as reported in a previous OT study (29).

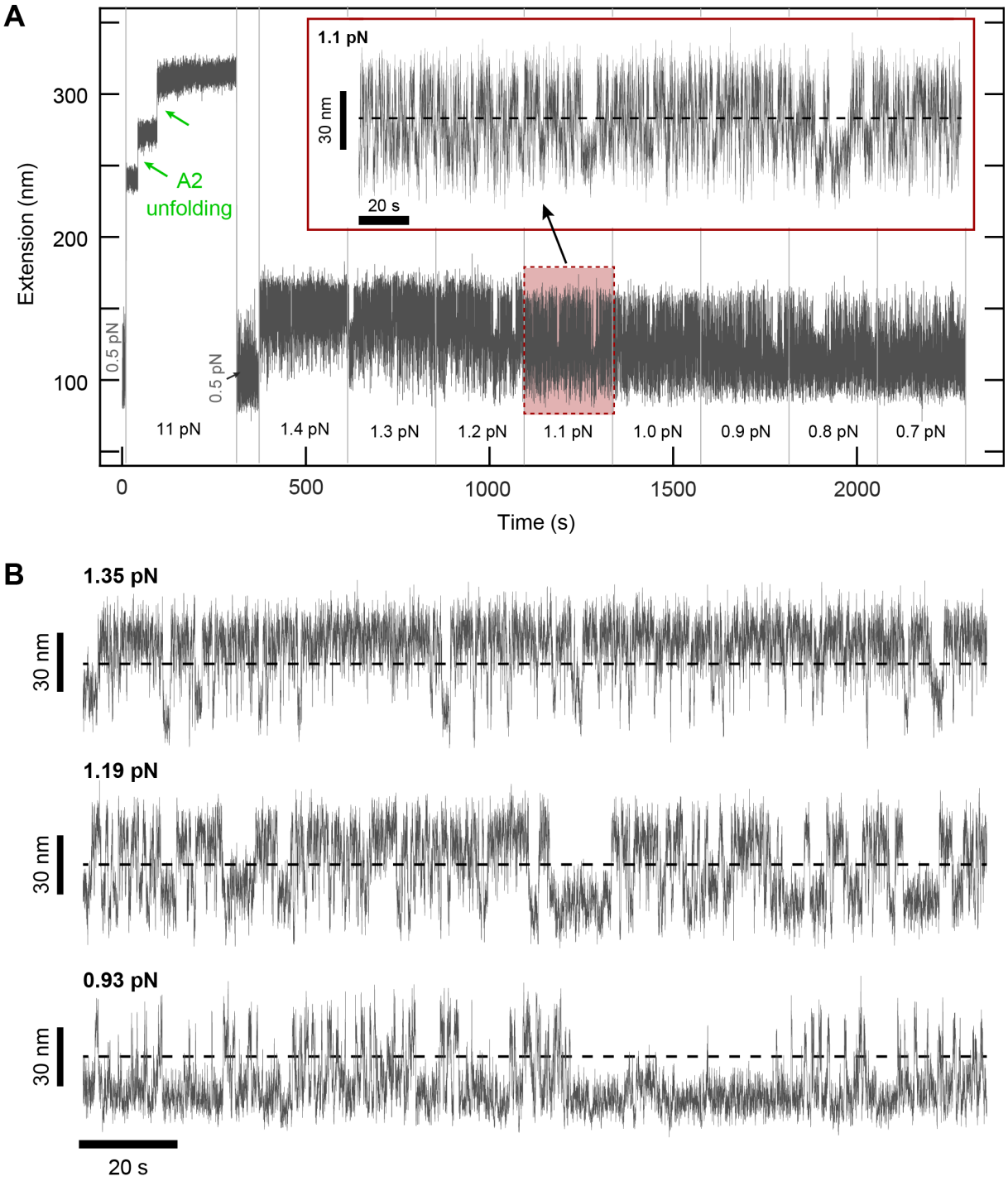

Fig. S16. VWF stem unzipping and zipping at low force. (A) Full trace of the VWF dimer tether presented in Fig. 6 in the main text. After fingerprint A2 domain unfolding at 11 pN (green arrows) and refolding at 0.5 pN, the tether is subjected to stepwise decreasing low forces between 1.4 and 0.7 pN for 240 s each. Fast reversible transitions to multiple extension levels between a maximum and minimum value of extension, approximately 60 nm apart, are observed that we attribute to closing and opening transitions of the C-domain stem. The inset shows the 240 s-long segment at 1.1 pN. The dashed line indicates the midpoint between the two extreme values of extension. **(B)** Extension *vs*. time traces of a VWF tether from a different flow cell, again exhibiting fast transitions at forces of ~1 pN, with the population being shifted towards higher tether extensions for higher forces. Dashed lines indicate the midpoint between the two extreme values of extension.

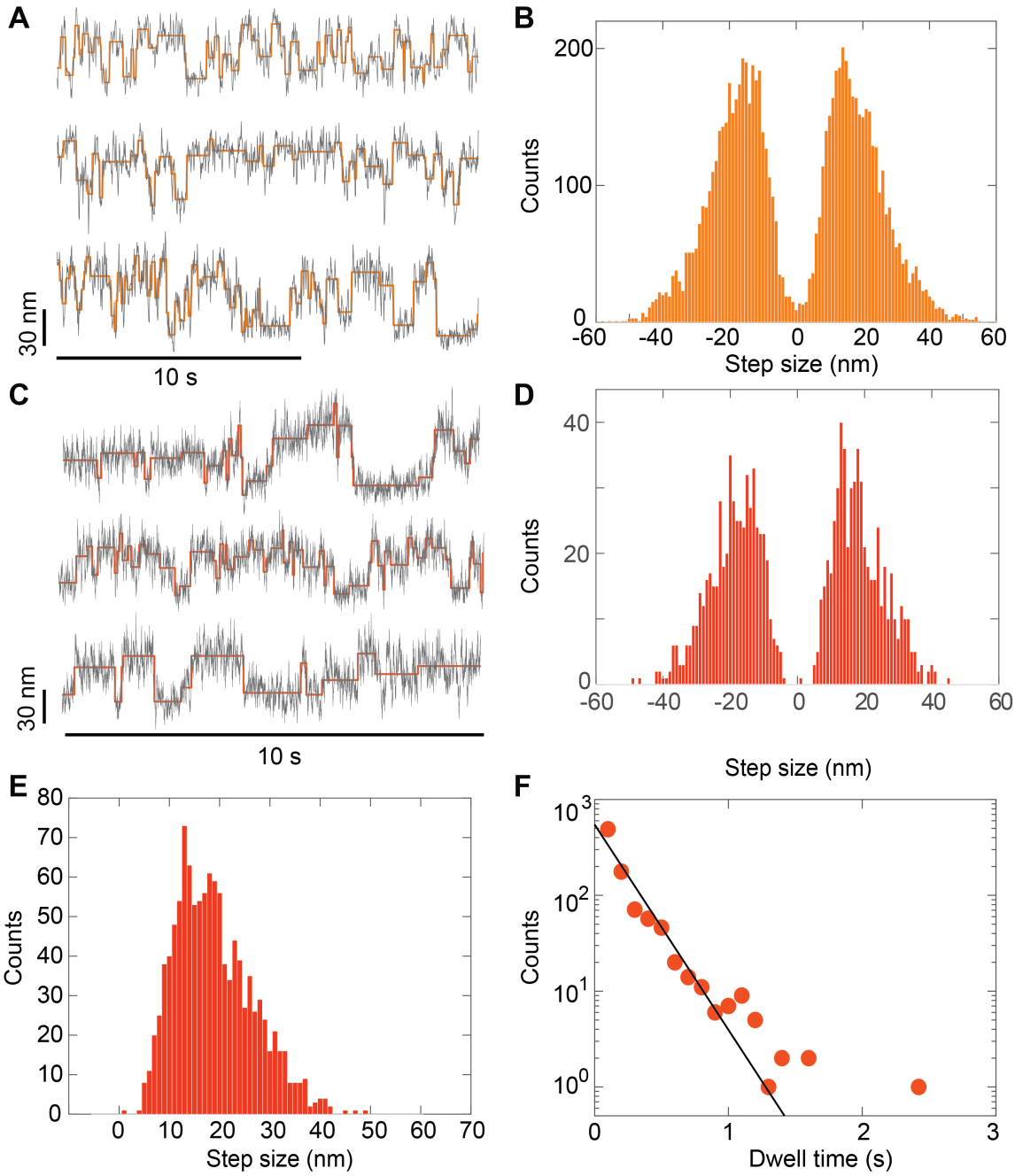

Fig. S17. Quantification of fast transitions in the VWF stem at low forces. (A) Extension time traces for VWF dimer constructs recorded close to $F_{1/2}$ at 58 Hz. Raw data (thin grey lines) and steps determined using a step finding algorithm (19) (orange lines). These data are recorded for different molecules, but otherwise essentially identical to the traces in Fig. 7A. **(B)** Distribution of step sizes. These are the same data as shown in Fig. 7B (7659 steps in total, all from data recorded at 58 Hz), but distinguishing between positive (up) and negative (down) steps. **(C)** Extension time traces for VWF dimer constructs recorded at 1.3 pN and with a camera frequency of 1 kHz. Raw data (thin grey lines) and steps determined using a step finding algorithm (red lines). **(D)** Distribution of step sizes determined from extension traces recorded at 1 kHz close to $F_{1/2}$. **(E)** Distribution of the magnitude of steps sizes from extension traces recorded at 1 kHz. **(F)** Distribution of dwell times from traces recorded at 1 kHz (red circles). The black line is a maximum likelihood fit of a single exponential model to the data with τ = 0.20 s ± 0.01 s (mean ± 95% CI). The total number of steps in the data set shown panels D, E, and F is 1113.

Supporting References

1. Yin J, et al. (2005) Genetically encoded short peptide tag for versatile protein labeling by Sfp phosphopantetheinyl transferase. *Proc Natl Acad Sci* 102(44):15815–15820.
2. Gibson DG, et al. (2009) Enzymatic assembly of DNA molecules up to several hundred kilobases. *Nat Methods* 6(5):343–345.
3. Milles LF, Bayer EA, Nash MA, Gaub HE (2017) Mechanical Stability of a High-Affinity Toxin Anchor from the Pathogen *Clostridium perfringens*. *J Phys Chem B* 121(15):3620–3625.
4. Schmidt TG, Skerra A (2007) The Strep-tag system for one-step purification and high-affinity detection or capturing of proteins. *Nat Protoc* 2(6):1528–1535.
5. Phan J, et al. (2002) Structural basis for the substrate specificity of tobacco etch virus protease. *J Biol Chem* 277(52):50564–72.
6. Theile CS, et al. (2013) Site-specific N-terminal labeling of proteins using sortase-mediated reactions. *Nat Protoc* 8(9):1800–7.
7. Müller JP, et al. (2016) Force Sensing by the Vascular Protein von Willebrand Factor is Tuned by a Strong Intermonomer Interaction. *Proc Natl Acad Sci* 113(5):1208–1213.
8. Müller JP, et al. (2016) pH-dependent interactions in dimers govern the mechanics and structure of von Willebrand Factor. *Biophys J* 111(2):312–322.
9. Ott W, et al. (2017) Elastin-like Polypeptide Linkers for Single-Molecule Force Spectroscopy. *ACS Nano* 11(6):6346–6354.
10. Ott W, Nicolaus T, Gaub HE, Nash MA (2016) Sequence-Independent Cloning and Post-Translational Modification of Repetitive Protein Polymers through Sortase and Sfp-Mediated Enzymatic Ligation. *Biomacromolecules* 17(4):1330–1338.
11. Sedlak SM, et al. (2017) Monodisperse measurement of the biotin-streptavidin interaction strength in a well-defined pulling geometry. *PLoS One* 12(12):e0188722.
12. Sedlak SM, et al. (2018) Direction Matters: Monovalent Streptavidin/Biotin Complex under Load. *Nano Lett*:acs.nanolett.8b04045.
13. Walker PU, Vanderlinden W, Lipfert J (2018) Dynamics and energy landscape of DNA plectoneme nucleation. *Phys Rev E* 98(4):042412.
14. Lipfert J, Hao X, Dekker NH (2009) Quantitative modeling and optimization of magnetic tweezers. *Biophys J* 96(12):5040–9.
15. Cnossen JP, Dulin D, Dekker NH (2014) An optimized software framework for real-time, high-throughput tracking of spherical beads. *Rev Sci Instrum* 85(10):103712.
16. Te Velthuis AJW, Kerssemakers JWJ, Lipfert J, Dekker NH (2010) Quantitative guidelines for force calibration through spectral analysis of magnetic tweezers data. *Biophys J* 99(4):1292–302.
17. De Vlaminck I, Henighan T, van Loenhout MTJ, Burnham DR, Dekker C (2012) Magnetic Forces and DNA Mechanics in Multiplexed Magnetic Tweezers. *PLoS One* 7(8):e41432.
18. Ostrofet E, Papini FS, Dulin D (2018) Correction-free force calibration for magnetic tweezers experiments. *Sci Rep* 8(1):15920.
19. Kerssemakers JWJ, et al. (2006) Assembly dynamics of microtubules at molecular resolution. *Nature* 442(7103):709–712.
20. Petrosyan R (2017) Improved approximations for some polymer extension models. *Rheol Acta* 56(1):21–26.
21. Schwaiger I, Schleicher M, Noegel AA, Rief M (2005) The folding pathway of a fast-folding immunoglobulin domain revealed by single-molecule mechanical experiments. *EMBO Rep* 6(1):46–51.
22. Ott W, Jobst MA, Schoeler C, Gaub HE, Nash MA (2017) Single-molecule force spectroscopy on polyproteins and receptor–ligand complexes: The current toolbox. *J Struct Biol* 197(1):3–12.
23. Milles LF, Schulten K, Gaub HE, Bernardi RC (2018) Molecular mechanism of extreme mechanostability in a pathogen adhesin. *Science* 359(6383):1527–1533.
24. Vilfan ID, Lipfert J, Koster DA, Lemay SG, Dekker NH (2009) Magnetic Tweezers for Single-Molecule Experiments. *Handbook of Single-Molecule Biophysics* (Springer US, New York, NY), pp 371–395.
25. Bouchiat C, et al. (1999) Estimating the persistence length of a worm-like chain molecule from

force-extension measurements. *Biophys J* 76(1 Pt 1):409–13.
26. Allan DW (1966) Statistics of atomic frequency standards. *Proc IEEE* 54(2):221–230.
27. Czerwinski F, Richardson AC, Oddershede LB (2009) Quantifying Noise in Optical Tweezers by Allan Variance. *Opt Express* 17(15):13255.
28. van Oene MM, et al. (2018) Quantifying the Precision of Single-Molecule Torque and Twist Measurements Using Allan Variance. *Biophys J* 114(8):1970–1979.
29. Zhang X, Halvorsen K, Zhang C-Z, Wong WP, Springer TA (2009) Mechanoenzymatic Cleavage of the Ultralarge Vascular Protein von Willebrand Factor. *Science* 324:1330–1334.